Journal of Marine Science and Application (2019) 18:213–227
https://doi.org/10.1007/s11804-018-0037-1

RESEARCH ARTICLE

Robust Modeling, Sliding-Mode Controller, and Simulation of an Underactuated ROV Under Parametric Uncertainties and Disturbances

Mostafa Eslami[1] · Cheng Siong Chin[2] · Amin Nobakhti[1]

Received: 12 December 2017 / Accepted: 4 April 2018 / Published online: 24 September 2018

Abstract
A dynamic model of a remotely operated vehicle (ROV) is developed. The hydrodynamic damping coefficients are estimated using a semi-predictive approach and computational fluid dynamic software ANSYS-CFX™ and WAMIT™. A sliding-mode controller (SMC) is then designed for the ROV model. The controller is subsequently robustified against modeling uncertainties, disturbances, and measurement errors. It is shown that when the system is subjected to bounded uncertainties, the SMC will preserve stability and tracking response. The paper ends with simulation results for a variety of conditions such as disturbances and parametric uncertainties.

Keywords Remotely operated vehicle · Robust modeling · Sliding-mode control · Simulation · Disturbances · Parametric uncertainties

1 Introduction

Underwater robotic vehicles (URV) are broadly classified into remotely operated vehicles (ROV) and autonomous underwater vehicles (AUV) (Monroy et al. 2017; Shen et al. 2017a). They are used in the offshore oil industry for tasks such as installation of structures and pipelines, salvage, mine hunting, and other applications, where their endurance, economy, and safety makes them an obvious replacement for divers (Shen et al. 2017b; Vasilijevic et al. 2017). Due to its hard-wire link or tethered design, ROVs are best suited for work that involves real-time image transmission, operating from a stationary point or cruising at relatively slow speeds, such as in pipeline inspection. While the governing dynamics of underwater vehicles are generally understood, they are practically intractable. The problem stems from significant nonlinearities and modeling uncertainties (McLain and Rock 1996; Caccia et al. 2000; Chin and Lin 2018) and major hydrodynamic and inertial nonlinearities due to the inherent open-frame structure of the ROV. This is in contrast to AUVs which are designed to contain most equipment and are streamlined for faster maneuvering (Fossen 1994).

There are two established modeling approaches for ROVs (Shi et al. 2017): (1) predictive methods based on either computational fluid dynamics (CFD) or strip theory (Ferziger and Perić 2002; Wilson et al. 2006) and (2) experimental techniques. The ROV's dynamics is determined using test equipment such as the Planar Motion Mechanism (PMM) and Marine Dynamic Test Facility (Williams et al. 2000). Physical tests during design and prototyping usually take the form of small-scale testing (Chin et al. 2011). For truly accurate results, experimental model data are then referenced against computer simulation models obtained via computational fluid dynamic. Accordingly, in this paper, a dynamic model of the ROV is obtained from both CFD and experimental techniques (Chin et al. 2011; Koh et al. 2002) (verified by pool and water tank tests at the Nanyang Technological University).

The objective of the ROV control system is to keep both its velocity and position at the desired values. The ROV should adhere to these desirables even when the vessel is under the influence of (bounded) disturbances and measurement errors. Sliding-mode controller (SMC) has two important properties which are of significance in this case (Medina et al. 2016). Firstly, since the dynamics of the ROV are highly nonlinear with respect to both its position and velocity, using SMC

✉ Cheng Siong Chin
cheng.chin@newcastle.ac.uk

[1] Electrical Engineering Department, Sharif University of Technology, Azadi Avenue, Tehran 11365-11155, Iran

[2] Newcastle University Singapore, Singapore 599493, Singapore

means that a single controller can accommodate for the entire mission. Secondly, when the uncertainties are bounded, the SMC can be robustly designed to maintain stability and to ensure good tracking (Slotine and Li 1991; Khalil 2002).

The application of SMC to control of AUVs and fully actuated ROVs is not new (e.g., see Chin and Lin 2018; Valdovinos et al. 2009; Vázquez et al. 2017). Traditionally, the uncertainties are assumed to have a known structure and unknown parameters. The SMC law is then made adaptive to cater for their presence. The main advantage of adaptation is that the uncertainties do not have to be bounded. However, adaptation does have major drawbacks in practical applications. Firstly, the control law becomes more complex, leading to notably increased computation. Since onboard processing power is limited, increased computational costs will result in an increase of the control update intervals (sample time). Secondly, adaption of the control law will inherently take a finite amount of time, rendering a response to fast changing dynamics due to disturbances very difficult, if not impossible (Nicholas et al. 2015). Finally, successfully adaptive control needs persistent excitation which in practice can be quite exhaustive for hardware. In addition, the adaptive control of ROV can be difficult to control for underactuated system.

Accordingly, this work follows an alternative framework in which a non-adaptive SMC law is made robust against uncertainties with a known bound for underactuated system. This requires that the bound of uncertainties is known, similar to traditional robust control theory (Skogestad and Postlethwaite 2005; Burkan and Uzmay 2003). To determine the bound of the uncertainties, a detailed analysis of environmental disturbances (Antonelli et al. 2001) and modeling and measurement errors is carried out. The types of uncertainties considered in this paper are parametric uncertainties (modeling error), environmental disturbances (wind-generated wave and ocean currents), and measurement error in sensing devices. These are essentially all possible environmental and non-environmental uncertainties which may decrease performance of the controller in real life. To determine the bound of the uncertainties, a detailed analysis of environmental disturbances and modeling and measurement errors is carried out. The bounds are then verified through simulation of the real-life model of the ROV. Subsequently, the SMC is designed to accommodate the computed bounds. Backed by extensive simulation of the ROV with the proposed robust-SMC controller on a path-following mission, we demonstrate that the controller exhibits excellent performance, while respecting the design and physical constraints. This remains so, even in the presence of noticeable disturbances.

The summary of the contributions of the paper are as follows. First is the use of a non-adaptive-based sliding-mode controller for an underactuated ROV system in earth-fixed frame instead of a fully actuated one. Second is the simultaneous bound of parametric uncertainties due to model error and external disturbances due to wind and underwater current are determined for the resulting underactuated system.

2 Modeling

The ROV, designed by the Robotics Research Center (RRC) in Nanyang Technological University (NTU), RRC ROV is used to perform underwater pipeline inspections such as locating pipe leakages or cracks. The twin "eye-ball" ROV has an open-frame structure and is 1 m long, 0.9 m wide, and 0.9 m high. It has a dry weight of 1243 N and a current operating depth of 100 to 300 m. The RRC ROV has four 150-N-rated thruster inputs for six degree of freedom (DOF) (surge, sway, heave, roll, pitch, and yaw velocity). Roll and pitch motions are designed to be self-stabilizable, i.e., the center of buoyancy is located above the center of gravity. To proceed with modeling, the following are assumed in this paper:

(a) ROV is a rigid body and is fully submerged once in the water.
(b) Water is assumed incompressible, viscid, and irrotational.
(c) The earth-fixed frame of reference is inertial.
(d) Tether effects (Jordán and Bustamante 2007) attached to the ROV is not modeled (assuming light weight, neutrally buoyant, and there is sufficient slack so that minimal disturbance loads are transmitted to the vehicle).

2.1 ROV Equations of Motion

For marine vehicles, six DOFs are conventionally defined by the following vectors (Fossen 1994):

- $\boldsymbol{\eta} = \left[\boldsymbol{\eta}_1^{\mathrm{T}} \ \boldsymbol{\eta}_2^{\mathrm{T}}\right]^{\mathrm{T}} = [x \ y \ z \ \phi \ \theta \ \psi]^{\mathrm{T}}$ —position and orientation (Euler angles) in inertia frame
- $\boldsymbol{\nu} = \left[\boldsymbol{\nu}_1^{\mathrm{T}} \ \boldsymbol{\nu}_2^{\mathrm{T}}\right]^{\mathrm{T}} = [u \ v \ w \ p \ q \ r]^{\mathrm{T}}$ —linear and angular velocities in body-fixed frame
- $\boldsymbol{\tau} = \left[\boldsymbol{\tau}_1^{\mathrm{T}} \ \boldsymbol{\tau}_2^{\mathrm{T}}\right]^{\mathrm{T}} = \left[\tau_x \ \tau_y \ \tau_z \ \tau_\phi \ \tau_\theta \ \tau_\psi\right]^{\mathrm{T}}$ —forces and moments acting on the vehicle in body-fixed frame

A rigid-body ROV's dynamic equation of motion is usually expressed in the body-fixed frame as the forces and measurement devices are intuitively related to this body frame of reference. Using the Newtonian approach, the motion is described by the following equation (Fossen 1994):

$$\boldsymbol{M}_{\mathrm{RB}}\dot{\boldsymbol{\nu}} + \boldsymbol{C}_{\mathrm{RB}}(\boldsymbol{\nu})\boldsymbol{\nu} = \boldsymbol{\tau}_{\mathrm{RB}} \tag{1}$$

where $\boldsymbol{M}_{\mathrm{RB}} \in R^{6\times 6}$ is the mass inertia matrix, $\boldsymbol{C}_{\mathrm{RB}}(\boldsymbol{\nu}) \in R^{6\times 6}$ is the rigid-boy Coriolis and centripetal matrix, and $\boldsymbol{\tau}_{\mathrm{RB}} \in R^{6\times 1}$ is

the external forces and moments vector. The mass inertia matrix is

$$\boldsymbol{M}_{\mathrm{RB}} = \begin{bmatrix} m & 0 & 0 & 0 & mz_G & -my_G \\ 0 & m & 0 & -mz_G & 0 & mx_G \\ 0 & 0 & m & my_G & -mx_G & 0 \\ 0 & -mz_G & my_G & I_x & -I_{xy} & -I_{xz} \\ mz_G & 0 & -mx_G & -I_{yx} & I_y & -I_{yz} \\ -my_G & mx_G & 0 & -I_{zx} & -I_{zy} & I_z \end{bmatrix} \tag{2}$$

The Coriolis and centripetal terms, describing the angular motion of the ROV, are

$$\boldsymbol{C}_{\mathrm{RB}}(\boldsymbol{\nu}) = \begin{bmatrix} \mathbf{0}_{3\times 3} & \boldsymbol{C}_{12}(\boldsymbol{\nu}) \\ -\boldsymbol{C}_{12}^{\mathrm{T}}(\boldsymbol{\nu}) & \boldsymbol{C}_{22}(\boldsymbol{\nu}) \end{bmatrix} \tag{3}$$

with

$$\boldsymbol{C}_{12}(\boldsymbol{\nu}) = \begin{bmatrix} m(y_G q + z_G r) & -m(x_G q - w) & -m(x_G r + v) \\ -m(y_G p + w) & m(z_G r + x_G p) & -m(y_G r - u) \\ -m(z_G p - v) & -m(z_G q + u) & m(x_G p + y_G q) \end{bmatrix} \tag{4}$$

$$\boldsymbol{C}_{22}(\boldsymbol{\nu}) = \begin{bmatrix} 0 & -I_{yz}q - I_{xz}p + I_z r & I_{yz}r + I_{xy}p - I_y q \\ I_{yz}q + I_{xz}p - I_z r & 0 & -I_{xz}r - I_{xy}q + I_x p \\ -I_{yz}r - I_{xy}p + I_y q & I_{xz}r + I_{xy}q - I_x p & 0 \end{bmatrix} \tag{5}$$

The external force and moment vector includes the hydrodynamic forces and moments due to damping and inertial of surrounding fluid known as added mass, and restoring force and moment. These forces and moments tend to oppose the motion of the ROV. Thus, the model can be expressed with respect to a local body-fixed reference frame, in the following matrix form (Fossen 1994):

$$\begin{aligned} M\dot{\nu} + C(\nu)\nu + D(\nu)\nu + g(\eta) &= \tau \\ \dot{\eta} &= J(\eta_2)\nu \\ \nu &= J^{-1}(\eta_2)\dot{\eta} \end{aligned} \tag{6}$$

where $\boldsymbol{M} = \boldsymbol{M}_{\mathrm{RB}} + \boldsymbol{M}_{\mathrm{A}} \in R^{6\times 6}$ is the inertia matrix for rigid body and added mass, respectively, $\boldsymbol{C}(\boldsymbol{\nu}) = \boldsymbol{C}_{\mathrm{RB}}(\boldsymbol{\nu}) + \boldsymbol{C}_{\mathrm{A}}(\boldsymbol{\nu}) \in R^{6\times 6}$ is the rigid-body and hydrodynamic rigid-body Coriolis and centripetal matrix, respectively, and $\boldsymbol{D}(\boldsymbol{\nu}) = \boldsymbol{D}_L + \boldsymbol{D}_Q(\boldsymbol{\nu}) \in R^{6\times 6}$ is the linear and quadratic damping matrix respectively. The input force and moment vector $\boldsymbol{\tau} = \boldsymbol{T}\boldsymbol{\sigma} \in R^6$ relate the thrust output vector $\boldsymbol{\sigma} = \boldsymbol{F}_T\overline{\boldsymbol{\sigma}} \in R^4$ with the thruster configuration matrix $\boldsymbol{T} \in R^{6\times 4}$, and $\boldsymbol{F}_T \in R^{4\times 4}$ is the dynamics of each thruster that converts the input voltage command $\overline{\boldsymbol{\sigma}} \in R^4$ into thrust to propel the vehicle. $\boldsymbol{J}(\boldsymbol{\eta_2})$ is the Euler transformation (ET) matrix which brings the inertia frame into alignment with the body-fixed frame and $\boldsymbol{J}^{-1}(\boldsymbol{\eta_2})$ is the inverse Euler transformation (IET) matrix which brings the body-fixed frame into alignment with the inertial frame

$$\boldsymbol{J}(\boldsymbol{\eta_2}) = \begin{bmatrix} \boldsymbol{J}_1(\boldsymbol{\eta_2}) & 0 \\ 0 & \boldsymbol{J}_2(\boldsymbol{\eta_2}) \end{bmatrix} \tag{7}$$

$$\boldsymbol{J}^{-1}(\boldsymbol{\eta_2}) = \begin{bmatrix} \boldsymbol{J}_1^{-1}(\boldsymbol{\eta_2}) & 0 \\ 0 & \boldsymbol{J}_2^{-1}(\boldsymbol{\eta_2}) \end{bmatrix}$$

and

$$\boldsymbol{J}_1(\boldsymbol{\eta_2}) = \begin{bmatrix} c(\psi)c(\theta) & -s(\psi)c(\phi) + c(\psi)s(\theta)s(\phi) & s(\psi)s(\phi) + c(\psi)c(\phi)s(\theta) \\ s(\psi)c(\theta) & c(\psi)c(\phi) + s(\phi)s(\theta)s(\psi) & -c(\psi)s(\phi) + s(\theta)s(\psi)c(\phi) \\ -s(\theta) & c(\theta)s(\phi) & c(\theta)c(\phi) \end{bmatrix}$$

$$\boldsymbol{J}_1^{-1}(\boldsymbol{\eta_2}) = \boldsymbol{J}_1^{\mathrm{T}}(\boldsymbol{\eta_2})$$

$$\boldsymbol{J}_2(\boldsymbol{\eta_2}) = \begin{bmatrix} 1 & s(\phi)t(\theta) & c(\phi)t(\theta) \\ 0 & c(\phi) & -s(\phi) \\ 0 & \frac{s(\phi)}{c(\theta)} & \frac{c(\phi)}{c(\theta)} \end{bmatrix}, \quad \boldsymbol{J}_2^{-1}(\boldsymbol{\eta_2}) = \begin{bmatrix} 1 & 0 & -s(\theta) \\ 0 & c(\phi) & c(\theta)s(\phi) \\ 0 & -s(\phi) & c(\theta)c(\phi) \end{bmatrix}$$

where $s(.) = \sin(.)$, $c(.) = \cos(.)$, and $t(.) = \tan(.)$. The ET is undefined for $\theta = \pm\pi/2$. However, this will not pose a problem since the vehicle is not designed or required to pitch anywhere near $\pm\pi/2$, in other words $c(\theta) \neq 0$. By this fact, both ET and IET are nonsingular (full rank) for all $\boldsymbol{\eta_2} \in R^3$. Note that in this approach matrix, $\dot{\boldsymbol{M}} - 2\boldsymbol{C}(\boldsymbol{\nu})$ is skew symmetric, i.e., for any $\boldsymbol{x} \in R^6$, we have $\boldsymbol{x}^{\mathrm{T}}(\boldsymbol{M}^{\cdot} - 2\boldsymbol{C}(\boldsymbol{\nu}))\,\boldsymbol{x} = 0$.

2.2 Gravitational and Buoyancy Forces

The term $\boldsymbol{g}(\boldsymbol{\eta})$ is used to describe the gravitational and buoyancy forces vector exerted on the ROV in the water (Fossen 1994). The gravitational and buoyancy forces are functions of the orientation and are independent of vehicle motion. When fully submerged, the ROV's buoyancy is equal to the weight of water displaced, i.e., $B = \rho g \nabla$ where ρ is the fluid density, ∇ is the volume displaced by the submerged ROV and g is the earth gravitational constant equal to 9.8(m/sec^2). In the body-fixed coordinate system, the restoring force vector becomes

$$\boldsymbol{g}(\boldsymbol{\eta}) = \begin{bmatrix} (W-B)s(\theta) \\ -(W-B)c(\theta)s(\phi) \\ -(W-B)c(\theta)c(\phi) \\ -(y_G W - y_B B)c(\theta)c(\phi) + (z_G W - z_B B)c(\theta)s(\phi) \\ (z_G w - z_B B)s(\theta) + (x_G W - x_B B)c(\theta)c(\phi) \\ -(x_G W - x_B B)c(\theta)s(\phi) - (y_G W - y_B B)s(\theta) \end{bmatrix} \tag{8}$$

As the ROV is neutrally buoyant, then $W = B$. By appropriately placing the additional mass on the ROV, the XY

coordinates of the center of buoyancy will coincide with the XY coordinate of the center of gravity, that is $x_G = x_B = 0$ and $y_G = y_B = 0$. Then, Eq. (8) becomes

$$\boldsymbol{g}^{\mathrm{T}}(\boldsymbol{\eta}) = [0 \;\; 0 \;\; 0 \;\; (z_G - z_B)Wc(\theta)s(\phi) \;\; (z_G - z_B)Ws(\theta) \;\; 0] \quad (9)$$

2.3 Hydrodynamic Derivatives

In the vehicle equations of motion (6), external forces and moments such as hydrodynamic drag force, actuator thrust, and hydrodynamic added mass forces are described in terms of vehicle's corresponding hydrodynamic coefficients. These coefficients are expressed in the form of hydrodynamic derivatives which are in accordance with the SNAME (1950) notation. For example, axial quadratic drag force is modeled as

$$X = -\left(\frac{1}{2}\rho C_d A\right)u|u| = X_{u|u|}u|u| \quad (10)$$

which implies that the drag force derivative in the surge direction with respect to $u \mid u \mid$ is

$$X_{u|u|} = \frac{\partial X}{\partial(u|u|)} = -\frac{1}{2}\rho C_d A \quad (11)$$

Since the RRC ROV is symmetric about the XZ plane and close to symmetric about YZ plane, it is assumed that the motions in surge, sway, pitch, and yaw are decoupled (Fossen 1994). Although it is not symmetric about the XY plane, the surge and heave motions are considered to be decoupled. Besides, the vehicle is designed to operate at relatively low speeds in which the nonlinear or quadratic effects can be small and assumed negligible. With this assumption, the drag matrix in (6) becomes

$$\boldsymbol{D} = \mathrm{diag}\left(\begin{bmatrix} X_u & Y_v & Z_w & K_p & M_q & N_r \end{bmatrix}\right) \quad (12)$$

where X_u is the damping coefficient for x-direction, Y_v is the damping coefficient for y-direction, and so forth.

The relationship between the hydrodynamic forces, moments, and accelerations are represented by added mass. For example, if there is acceleration $\dot{u}$ in the X direction, the hydrodynamic force X arising from that motion can be taken as $X = X_{\dot{u}}\dot{u}$ where $X_{\dot{u}} = \partial X/\partial \dot{u}$ is the hydrodynamic derivative. For most low-speed underwater vehicles, the off-diagonal terms of $\boldsymbol{M}_A$ are often neglected (Fossen 1994) leading to

$$\boldsymbol{M}_{\mathrm{A}} = \mathrm{diag}\left(\begin{bmatrix} X_{\dot{u}} & Y_{\dot{v}} & Z_{\dot{w}} & K_{\dot{p}} & M_{\dot{q}} & N_{\dot{p}} \end{bmatrix}\right) \quad (13)$$

The corresponding Coriolis and centripetal added mass matrix $\boldsymbol{C}_{\mathrm{A}}(\boldsymbol{v})$ becomes

$$\boldsymbol{C}_A(\boldsymbol{v}) = \begin{bmatrix} 0 & 0 & 0 & 0 & -Z_{\dot{w}}w & Y_{\dot{v}}v \\ 0 & 0 & 0 & Z_{\dot{w}}w & 0 & -X_{\dot{u}}u \\ 0 & 0 & 0 & -Y_{\dot{v}}v & X_{\dot{u}}u & 0 \\ -Z_{\dot{w}}w & Y_{\dot{v}}v & 0 & -N_{\dot{r}}r & -N_{\dot{r}}r & M_{\dot{q}}q \\ Z_{\dot{w}}w & 0 & -X_{\dot{u}}u & N_{\dot{r}}r & 0 & -K_{\dot{p}}p \\ -Y_{\dot{v}}v & X_{\dot{u}}u & 0 & -M_{\dot{q}}q & K_{\dot{p}}p & 0 \end{bmatrix} \quad (14)$$

The hydrodynamic damping forces were obtained via open-tank tests and ANSYS-CFX™ (see Fig. 1a) and were verified by comparing the results with a free-decaying experiment on a scaled RRC ROV model (see Fig. 1c). Note that in this approach matrix, $\dot{\boldsymbol{M}} - 2\boldsymbol{C}(\boldsymbol{\nu})$ is skew symmetric, i.e., for any $\boldsymbol{x} \in \mathscr{R}^6$, we have $\boldsymbol{x}^{\mathrm{T}}(\dot{\boldsymbol{M}} - 2\boldsymbol{C}(\boldsymbol{\nu}))\,\boldsymbol{x} = 0$.

By applying laws of similitude, the hydrodynamics parameters of the scaled model can be scaled up to predict the corresponding values of the actual RRC ROV model. The hydrodynamic added mass coefficients were obtained using MULTISURF™ and WAMIT™ as shown in Fig. 1b. The added mass coefficients obtained were similarly obtained. Full details of the CFD simulation and experimental tests used to determine the damping and added mass coefficient for the RRC ROV model can be found in (Chin et al. 2011) and the data are shown in Appendix Table 1.

2.4 Thrust Model

The position of the thruster on the ROV (see Fig. 2) is defined by the thrusters' configuration matrix, $\boldsymbol{T}$. The details of the steady-state experiment performed on the thruster can be found in Koh et al. (2002). The input forces and moments to the ROV are determined based on summation of the force and moment equations in the six DOFs

$$\boldsymbol{\tau} = \begin{bmatrix} \tau_x \\ \tau_y \\ \tau_z \\ \tau_\phi \\ \tau_\theta \\ \tau_\psi \end{bmatrix} = \begin{bmatrix} 1 & 1 & 0 & 0 \\ 0 & 0 & s(\beta) & -s(\beta) \\ 0 & 0 & c(\beta) & c(\beta) \\ 0 & 0 & \delta & \delta \\ -\varepsilon & -\varepsilon & \alpha c(\beta) & -\alpha c(\beta) \\ \gamma & -\gamma & \alpha s(\beta) & -\alpha s(\beta) \end{bmatrix} \begin{bmatrix} \sigma_1 \\ \sigma_2 \\ \sigma_3 \\ \sigma_4 \end{bmatrix} = \boldsymbol{T}\boldsymbol{\sigma} \quad (15)$$

where the α = 0.017m, $\beta = \pi/4$, γ = 0.31m, δ = 0.293m, and ε = 0.016m are the geometrical parameters based on the thrusters' location on the ROV platform (see Fig. 2), $\sigma_{\min} \le \sigma_i \le \sigma_{\max}$ i = 1,2,3,4 are the

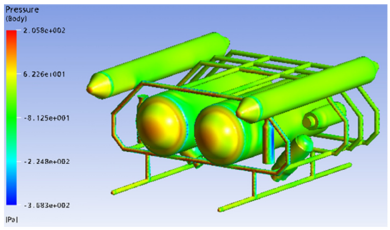

(a) Pressure distributions on the ROV Body using ANSYS-CFX™

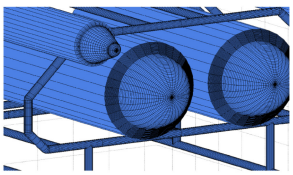

(b) WAMIT™ model used in added mass computation

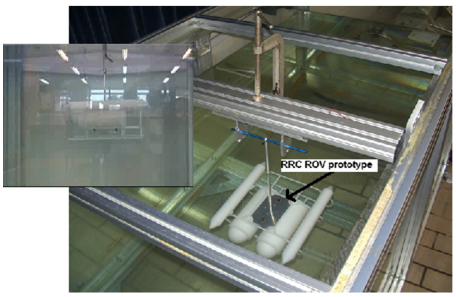

(c) RRC ROV prototype in water tank (orientated in surge direction)

Fig. 1 RRC ROV prototype used in simulation and testing. (**a**) Pressure distributions on the ROV Body using ANSYSCFX (**b**) WAMIT model used in added mass computation (**c**) RRC ROV prototype test in water tank

minimum and maximum thrust output by each thrusters and $\boldsymbol{\tau} = [\tau_x\ \tau_y\ \tau_z\ \tau_\phi\ \tau_\theta\ \tau_\psi]^T$ is the force and moment vector generated in the six DOFs. The input is $\boldsymbol{\sigma} = \boldsymbol{F}_T\ \overline{\boldsymbol{\sigma}} \in R^4$ with $\boldsymbol{F}_T = f_T \boldsymbol{I}_4$, and $\overline{\boldsymbol{\sigma}} \in R^4$ is the commanded voltage input to the thrusters. Note that due to the ROV configuration, the values of α and ε are small. Thus, roll and pitch (fourth and fifth equations) are not fully actuated and there are insufficient thrusters to fully maneuver the ROV in the six DOFs (ROV is underactuated).

Since the thrusters have a relatively shorter response time compared to the ROV, they may be modeled as gain terms (Koh et al. 2002). Lumped hydro-electromechanical dynamic model for both the DC motor shaft speed (assuming small electrical time constant as compared to the mechanical time constant) and propeller's dynamic were used. Experimental results indicate the approximate linear relationship between the thrust (σ_i) and the thruster input voltage ($\overline{\sigma}_i$) to be

$$\sigma_i = f_T \overline{\sigma}_i, \quad i = 1,\ 2,\ 3,\ \text{or}\ 4 \tag{16}$$

where f_T = 0.92 N m/V (forward thrust) and f_T = 0.61 N m/V (reverse thrust).

3 Design of the SMC Controller

3.1 Design Framework

The ROV equations of motion in the body-fixed frame are

$$\boldsymbol{M}\dot{\boldsymbol{v}} + \boldsymbol{C}(\boldsymbol{\nu})\boldsymbol{\nu} + \boldsymbol{D}\boldsymbol{\nu} + \boldsymbol{g}(\boldsymbol{\eta}) = \boldsymbol{\tau} \tag{17}$$

which compare to its earth-fixed equations given below,

$$\boldsymbol{M}_\eta(\boldsymbol{\eta})\,\ddot{\boldsymbol{\eta}} + \boldsymbol{C}_\eta(\boldsymbol{\eta},\boldsymbol{\nu})\,\dot{\boldsymbol{\eta}} + \boldsymbol{D}_\eta(\boldsymbol{\eta})\,\dot{\boldsymbol{\eta}} + \boldsymbol{g}_\eta(\boldsymbol{\eta}) = \boldsymbol{\tau}_\eta \tag{18}$$

where

$$\begin{aligned}
\boldsymbol{M}_\eta(\boldsymbol{\eta}) &= \boldsymbol{J}^{-\mathrm{T}}(\boldsymbol{\eta})\boldsymbol{M}\boldsymbol{J}^{-1}(\boldsymbol{\eta}) \\
\boldsymbol{C}_\eta(\boldsymbol{\eta},\boldsymbol{\nu}) &= \boldsymbol{J}^{-\mathrm{T}}(\boldsymbol{\eta})\left(\boldsymbol{C}(\boldsymbol{\nu}) - \boldsymbol{M}\boldsymbol{J}^{-1}(\boldsymbol{\eta})\dot{\boldsymbol{J}}(\boldsymbol{\eta})\right)\boldsymbol{J}^{-1}(\boldsymbol{\eta}) \\
\boldsymbol{D}_\eta(\boldsymbol{\eta}) &= \boldsymbol{J}^{-\mathrm{T}}(\boldsymbol{\eta})\boldsymbol{D}\boldsymbol{J}^{-1}(\boldsymbol{\eta}) \\
\boldsymbol{g}_\eta(\boldsymbol{\eta}) &= \boldsymbol{J}^{-\mathrm{T}}(\boldsymbol{\eta})\boldsymbol{g}(\boldsymbol{\eta}) \\
\boldsymbol{\tau}_\eta &= \boldsymbol{J}^{-\mathrm{T}}(\boldsymbol{\eta})\boldsymbol{\tau}
\end{aligned}$$

Clearly, the model appears much simpler in the body-fixed frame, leading to less calculations. In addition, specifying the desired trajectory for ROVs is more natural in the body-fixed frame, as opposed to for AUVs for which it is more natural to use the earth-fixed frame. Nevertheless, in this instance, using the body frame to design the control law will lead to difficulties. In particular, it is demonstrated in Section 3.2 that computing the control law in the earth-fixed framework requires knowledge of $\boldsymbol{\eta}$ and $\dot{\boldsymbol{\eta}}$ for feedback purposes. In the body-fixed framework, these will change to $\int \boldsymbol{\nu}(t)\mathrm{d}t$ and $\boldsymbol{v}$, where $\int \boldsymbol{\nu}_2(t)\mathrm{d}t$ does not have a physical interpretation and it is not possible to integrate $\boldsymbol{\nu}_2$ (Fossen 1994). Therefore, in spite of its more complicated characteristics, the Earth-fixed frame is used for control system design. Note that translating the dynamic model of ROV from body-fixed frame into earth-fixed frame preserves the skew-symmetric property of $\dot{\boldsymbol{M}}_\eta(\boldsymbol{\eta}) - 2\boldsymbol{C}_\eta(\boldsymbol{\eta},\boldsymbol{\nu})$, since $\mathrm{d}\left(\boldsymbol{J}^{-1}(\boldsymbol{\eta})\right)/\mathrm{d}t = \boldsymbol{J}^{-1}(\boldsymbol{\eta})\,\dot{\boldsymbol{J}}(\boldsymbol{\eta})\boldsymbol{J}^{-1}(\boldsymbol{\eta})$ and

$$\begin{aligned}
&\dot{\boldsymbol{M}}_\eta(\boldsymbol{\eta}) = -2\dot{\boldsymbol{J}}^{-\mathrm{T}}(\boldsymbol{\eta})\boldsymbol{M}\boldsymbol{J}^{-1}(\boldsymbol{\eta})\,\dot{\boldsymbol{J}}(\boldsymbol{\eta})\boldsymbol{J}^{-1}(\boldsymbol{\eta}) \Rightarrow \\
&\dot{\boldsymbol{M}}_\eta(\boldsymbol{\eta}) - 2\boldsymbol{C}_\eta(\boldsymbol{\eta},\boldsymbol{\nu}) = \boldsymbol{J}^{-\mathrm{T}}(\boldsymbol{\eta})(\boldsymbol{M} - 2\boldsymbol{C}(\boldsymbol{\nu}))\boldsymbol{J}^{-1}(\boldsymbol{\eta})
\end{aligned} \tag{19}$$

3.2 Stability Performance of Sliding-Mode Controller

Given the disparity among the DOF (six) and the number of thrusters (four), movement in some degrees of freedom will require more than one active thruster. To optimally distribute actuation among the four thrusters, a least-squares optimization approach is employed. Let τ represent a vector of bounded torques. The unconstrained thrust allocation problem can be formulated as follows:

$$\min_{\sigma} \frac{1}{2}\boldsymbol{\sigma}^{\mathrm{T}}\boldsymbol{W}\boldsymbol{\sigma} \tag{20}$$

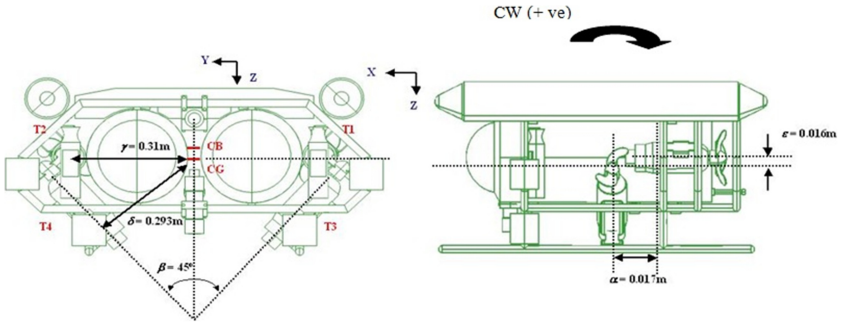

Fig. 2 Position of thrusters on the ROV

Subject to $\boldsymbol{\tau} - \boldsymbol{T}\boldsymbol{\sigma} = 0$ where $\boldsymbol{W}$ is a positive definite matrix. The solution using Lagrange multipliers is (Fossen 1994)

$$\boldsymbol{\sigma} = \boldsymbol{T}^{+}\boldsymbol{\tau} \tag{21}$$

where

$$\boldsymbol{T}^{+} = \boldsymbol{W}^{-1}\boldsymbol{T}^{\mathrm{T}}\left(\boldsymbol{T}\boldsymbol{W}^{-1}\boldsymbol{T}^{\mathrm{T}}\right)^{-1} \tag{22}$$

represents the generalized inverse. If $\boldsymbol{W} = \boldsymbol{I}$ (i.e., equally weighted control forces), then (22) reduces to the Moore-Penrose pseudo inverse: $\boldsymbol{T}^{+} = \boldsymbol{T}^{\mathrm{T}}(\boldsymbol{T}\boldsymbol{T}^{\mathrm{T}})^{-1}$.

Using Slotine's approach, and assuming the model parameters are known (i.e., $\boldsymbol{M}$, $\boldsymbol{C}(\boldsymbol{\nu})$, $\boldsymbol{D}$, and $\boldsymbol{g}(\boldsymbol{\eta})$), and the values of $\boldsymbol{\eta}$ and $\dot{\boldsymbol{\eta}}$ are available, the control law becomes (Islam and Liu 2011; Liang et al. 2016; Valdovinos et al. 2009)

$$\boldsymbol{\tau} = \boldsymbol{J}^{\mathrm{T}}(\boldsymbol{\eta})\left(\boldsymbol{M}_{\eta}(\boldsymbol{\eta})\,\dot{\vartheta} + \boldsymbol{C}_{\eta}(\boldsymbol{\eta},\boldsymbol{\nu})\vartheta + \boldsymbol{D}_{\eta}(\boldsymbol{\eta})\,\dot{\boldsymbol{\eta}} + \boldsymbol{g}_{\eta}(\boldsymbol{\eta}) - \boldsymbol{\Gamma}\boldsymbol{s}\right) \tag{23}$$

where

$$\vartheta = \dot{\boldsymbol{\eta}}_{d} - \boldsymbol{\Lambda}\,\tilde{\boldsymbol{\eta}} \quad , \quad \boldsymbol{s} = \dot{\boldsymbol{\eta}} - \vartheta \tag{24}$$

and $\tilde{\boldsymbol{\eta}} = \boldsymbol{\eta} - \boldsymbol{\eta}_{d}$ is the tracking error, and $\boldsymbol{\Lambda}$ and $\boldsymbol{\Gamma}$ are diagonal positive definite matrices (gain matrices) defined as

$$\boldsymbol{\Lambda} = \mathrm{diag}([\lambda_1 \;\; \lambda_2 \;\; \ldots \;\; \lambda_6]) \;\; \text{and} \tag{25}$$

$$\boldsymbol{\Gamma} = \mathrm{diag}([\gamma_1 \;\; \gamma_2 \;\; \ldots \;\; \gamma_6])$$

The closed-loop equation comprising the system and the Slotine controller becomes

$$\begin{aligned} &\boldsymbol{M}_{\eta}(\boldsymbol{\eta})\left(\ddot{\boldsymbol{\eta}} - \dot{\vartheta}\right) + \boldsymbol{C}_{\eta}(\boldsymbol{\eta},\boldsymbol{\nu})\left(\dot{\boldsymbol{\eta}} - \vartheta\right) + \boldsymbol{\Gamma}\boldsymbol{s} = 0 \;\Rightarrow \\ &\qquad \boldsymbol{M}_{\eta}(\boldsymbol{\eta})\,\dot{\boldsymbol{s}} + \boldsymbol{C}_{\eta}(\boldsymbol{\eta},\boldsymbol{\nu})\boldsymbol{s} + \boldsymbol{\Gamma}\boldsymbol{s} = 0 \end{aligned} \tag{26}$$

which describes a nonlinear ordinary differential equation with $\boldsymbol{s}$ as the variable. To determine closed-loop stability, $V = 0.5\boldsymbol{s}^{\mathrm{T}}\boldsymbol{M}_{\eta}(\boldsymbol{\eta})\boldsymbol{s}$ is chosen as the candidate Lyapunov function. Since $\dot{\boldsymbol{M}}_{\eta}(\boldsymbol{\eta}) - 2\boldsymbol{C}_{\eta}(\eta, \nu)$ is skew-symmetric matrix, this leads to

$$\dot{V} = -\boldsymbol{s}^{\mathrm{T}}\boldsymbol{\Gamma}\boldsymbol{s} \le 0 \Rightarrow \boldsymbol{s} \to 0 \Rightarrow \tilde{\boldsymbol{\eta}} \to 0 \Rightarrow \boldsymbol{\eta} \to \boldsymbol{\eta}_{d}, \dot{\tilde{\boldsymbol{\eta}}} \to 0 \Rightarrow \dot{\boldsymbol{\eta}} \to \dot{\boldsymbol{\eta}}_{d} \tag{27}$$

Selection of a suitable sliding surface is an important step in the design of the SMC controller. The manner of the selection of the sliding surface in this paper is as follows. First, a candidate Lyapunov function $V = 0.5\boldsymbol{s}^{\mathrm{T}}\boldsymbol{M}_{\eta}(\boldsymbol{\eta})\boldsymbol{s}$ is considered and the sliding surface is chosen such that as $\boldsymbol{s} \to 0$ then $\eta \to \eta_{d}$ and $\dot{\eta} \to \dot{\eta}_{d}$. The derivative of the candidate Lyapunov function V is computed as follows:

$$\dot{V} = \boldsymbol{s}^{\mathrm{T}}\boldsymbol{M}_{\eta}(\boldsymbol{\eta})\,\dot{\boldsymbol{s}} + 0.5\boldsymbol{s}^{\mathrm{T}}\dot{\boldsymbol{M}}_{\eta}(\boldsymbol{\eta})\boldsymbol{s} \tag{28}$$

Using the skew-symmetric property for $\dot{\boldsymbol{M}}_{\eta}(\boldsymbol{\eta}) - 2\boldsymbol{C}_{\eta}(\boldsymbol{\eta},\boldsymbol{\nu})$, we have

$$\dot{V} = \boldsymbol{s}^{\mathrm{T}}\left(\boldsymbol{M}_{\eta}(\boldsymbol{\eta})\,\dot{\boldsymbol{s}} + \boldsymbol{C}_{\eta}(\boldsymbol{\eta},\boldsymbol{\nu})\boldsymbol{s}\right) \tag{29}$$

For a suitable choice, let $\boldsymbol{s} = \dot{\boldsymbol{\eta}} - \vartheta$ and substitute this for $\boldsymbol{M}_{\eta}(\boldsymbol{\eta})\ddot{\boldsymbol{\eta}}$ in (18). The resulting equation for the input signal $\boldsymbol{\tau}_{\eta}$ may then be inserted in $\dot{V}$,

$$\begin{aligned} \dot{V} &= \boldsymbol{s}^{\mathrm{T}}\left(\boldsymbol{M}_{\eta}(\boldsymbol{\eta})\left(\ddot{\boldsymbol{\eta}} - \dot{\vartheta}\right) + \boldsymbol{C}_{\eta}(\boldsymbol{\eta},\boldsymbol{\nu})\boldsymbol{s}\right) \\ &= \boldsymbol{s}^{\mathrm{T}}\left(-\boldsymbol{M}_{\eta}(\boldsymbol{\eta})\dot{\vartheta} + \boldsymbol{\tau}_{\eta} - \boldsymbol{C}_{\eta}(\boldsymbol{\eta},\boldsymbol{\nu})\,\dot{\boldsymbol{\eta}} - \boldsymbol{D}_{\eta}(\boldsymbol{\eta})\,\dot{\boldsymbol{\eta}} - \boldsymbol{g}_{\eta}(\boldsymbol{\eta}) + \boldsymbol{C}_{\eta}(\boldsymbol{\eta},\boldsymbol{\nu})\boldsymbol{s}\right) \\ &= \boldsymbol{s}^{\mathrm{T}}\left(\underline{-\boldsymbol{M}_{\eta}(\boldsymbol{\eta})\,\dot{\vartheta}} + \boldsymbol{\tau}_{\eta} \underline{- \boldsymbol{C}_{\eta}(\boldsymbol{\eta},\boldsymbol{\nu})\vartheta - \boldsymbol{D}_{\eta}(\boldsymbol{\eta})\,\dot{\boldsymbol{\eta}} - \boldsymbol{g}_{\eta}(\boldsymbol{\eta})}\right) \end{aligned} \tag{30}$$

The aim is to select $\boldsymbol{\tau}_{\eta}$ such that underlined terms in the above equations cancel out and $\dot{V}$ becomes negative. A simple choice is (23). Finally, let $\vartheta = \dot{\boldsymbol{\eta}}_{d} - \boldsymbol{\Lambda}(\boldsymbol{\eta} - \boldsymbol{\eta}_{d})$ which yields $\boldsymbol{s} = (\dot{\boldsymbol{\eta}} - \dot{\boldsymbol{\eta}}_{d}) + \boldsymbol{\Lambda}(\boldsymbol{\eta} - \boldsymbol{\eta}_{d})$. The control law (23) implies $\dot{V} = -\boldsymbol{s}^{\mathrm{T}}\boldsymbol{\Gamma}\boldsymbol{s} < 0$ for $\boldsymbol{\Gamma} > 0$, and $\boldsymbol{s} \to 0$. From (27),

$$\underline{\lambda}(\Gamma)\,\|\boldsymbol{s}\|^{2} \le \boldsymbol{s}^{\mathrm{T}}\boldsymbol{\Gamma}\boldsymbol{s} \le \overline{\lambda}(\boldsymbol{\Gamma})\,\|\boldsymbol{s}\|^{2} \Rightarrow \dot{V} \le -\underline{\lambda}(\boldsymbol{\Gamma})\,\|\boldsymbol{s}\|^{2} \tag{31}$$

and since $V = 0.5\boldsymbol{s}^{\mathrm{T}}\boldsymbol{M}_{\eta}(\boldsymbol{\eta})\boldsymbol{s}$, then

$$\frac{1}{2}\underline{\lambda}\left(\boldsymbol{M}_{\eta}(\boldsymbol{\eta})\right)\|\boldsymbol{s}\|^{2} \le \frac{1}{2}\boldsymbol{s}^{\mathrm{T}}\boldsymbol{M}_{\eta}(\boldsymbol{\eta})\boldsymbol{s} \le \frac{1}{2}\overline{\lambda}\left(\boldsymbol{M}_{\eta}(\boldsymbol{\eta})\right)\|\boldsymbol{s}\|^{2} \tag{32}$$

From (31) and (32), one may conclude that

$$\dot{V} \leq -2\left(\frac{\underline{\lambda}(\boldsymbol{\Gamma})}{\overline{\lambda}(\boldsymbol{M})}\right)V \Rightarrow V(t) \leq V(0)\mathrm{e}^{-2\left(\frac{\underline{\lambda}(\boldsymbol{\Gamma})}{\overline{\lambda}(\mathbf{M})}\right)t} \tag{33}$$

where $V(0) = 0.5\boldsymbol{s}(0)^{\mathrm{T}}\boldsymbol{M}_{\eta}(\boldsymbol{\eta}(0))\boldsymbol{s}(0) \geq 0$. The role of $\underline{\lambda}(\boldsymbol{\Gamma})$ now becomes evident. By increasing its value, $V(t)$ can be made to converge to zero exponentially faster. Moreover, the eigenvalues λ_i control the speed at which the error is eliminated $\tilde{\boldsymbol{\eta}} \rightarrow 0$. To see this, consider

$$\boldsymbol{s} = \dot{\tilde{\boldsymbol{\eta}}} + \boldsymbol{\Lambda}\tilde{\boldsymbol{\eta}} \tag{34}$$

For each individual-loop one obtains,

$$s_i(t) = \dot{\tilde{\eta}}_i(t) + \lambda_i\tilde{\eta}_i(t), \quad i = 1, 2, \ldots, 6 \tag{35}$$

where $\boldsymbol{s} = [s_1, s_2, \ldots, s_6]^{\mathrm{T}}$. The Laplace transform of which gives

$$\begin{aligned} S_i(\mathrm{s}) &= \mathrm{s}\tilde{\Omega}_i(\mathrm{s}) + \lambda_i\tilde{\Omega}_i(\mathrm{s}) = (\mathrm{s}+\lambda_i)\tilde{\Omega}_i(\mathrm{s}) \Rightarrow \tilde{\Omega}_i(\mathrm{s}) \\ &= \frac{S_i(\mathrm{s})}{\mathrm{s}+\lambda_i} \end{aligned} \tag{36}$$

where $S_i(\mathrm{s}) = L\{s_i(t)\}$ and $\Omega\tilde{}_i(\mathrm{s}) = L\{\eta\tilde{}_i(t)\}$.

Accordingly, a larger λ_i will lead to a greater tracking performance (i.e., the errors converge to zero more quickly). While a larger value of λ_i and γ_i will lead to better performance, it may also lead to difficulties in practical implementation; using a large value of this, gains will increase the effect of measurement noises on the control law. In addition, it will lead to control signals which violate the maximum torque limits. Therefore in practice, there is an upper bound on λ_i and γ_i. The trade-off between the control system performance and torque is evident from the following relationship:

$$\begin{aligned} \vartheta &= \dot{\boldsymbol{\eta}}_d - \lambda\tilde{\boldsymbol{\eta}} \Rightarrow \|\vartheta\| \leq \|\dot{\boldsymbol{\eta}}_d\| + \overline{\lambda}(\boldsymbol{\Lambda})\|\tilde{\boldsymbol{\eta}}\| \\ \dot{\vartheta} &= \ddot{\boldsymbol{\eta}}_d - \boldsymbol{\Lambda}\dot{\tilde{\boldsymbol{\eta}}} \Rightarrow \|\dot{\vartheta}\| \leq \|\ddot{\boldsymbol{\eta}}_d\| + \overline{\lambda}(\boldsymbol{\Lambda})\|\dot{\tilde{\boldsymbol{\eta}}}\| \end{aligned} \tag{37}$$

Imposing the above inequalities on the control law leads to

$$\begin{aligned} \boldsymbol{\tau}_{\eta} \leq &\left\{\overline{\lambda}(\boldsymbol{M}_{\eta}(\boldsymbol{\eta}))\|\ddot{\boldsymbol{\eta}}_d\| + \|\boldsymbol{g}_{\eta}(\boldsymbol{\eta})\| + \|\boldsymbol{C}\left(\boldsymbol{\eta}, \boldsymbol{\nu}\right) + \boldsymbol{D}_{\eta}(\boldsymbol{\eta})\|\|\dot{\boldsymbol{\eta}}_d\|\right\} \\ &+\left\{\overline{\lambda}(\boldsymbol{M}_{\eta}(\boldsymbol{\eta}))\overline{\lambda}(\boldsymbol{\Lambda})\|\dot{\tilde{\boldsymbol{\eta}}}\| + \overline{\lambda}(\boldsymbol{\Lambda})\|\boldsymbol{C}\left(\boldsymbol{\eta}, \boldsymbol{\nu}\right) + \boldsymbol{D}_{\eta}(\boldsymbol{\eta})\|\|\tilde{\boldsymbol{\eta}}\| + \overline{\lambda}(\boldsymbol{\Gamma})\|\boldsymbol{s}\|\right\} \end{aligned} \tag{38}$$

Note the appearance of $\boldsymbol{\Lambda}$ and $\boldsymbol{\Gamma}$ in the second term of the inequality. From (38) and $\boldsymbol{\tau}_{\eta} = \boldsymbol{J}^{-\mathrm{T}}(\boldsymbol{\eta})\boldsymbol{\tau}$, it is clear that to reduce the upper torque bounds $\boldsymbol{\tau}$, $\boldsymbol{\Lambda}$ and $\boldsymbol{\Gamma}$ should have smaller eigenvalues.

3.3 Robustification of the Control Law to Disturbances and Uncertainties

The derived model for the ROV is expected to have some discrepancy with the actual dynamics of the ROV. Moreover, the ROV is subject to considerable environmental disturbances and external forces. These will include waves and ocean currents. To study the effects of these disturbances, let $\mathrm{d}(t)$ be an extra torque in (18) which denotes the sum of all possible external disturbances. As with the study of uncertain linear systems, the upper bound of $\mathrm{d}(t)$, i.e., $\|\mathrm{d}(t)\| \leq \chi$, is considered known. A major benefit of the SMC framework is that it is possible to robustify the controller against these uncertainties by an augmentation of the control law. By adding an extra term $\boldsymbol{u}_0 \in R^6$, the stability of the closed-loop system will be guaranteed in the presence of these uncertainties (Tang et al. 2018; Chiaverini et al. 2004; Effatnejad and Namvar 2009). Consider the ROV's equations of motion, subject to the uncertainty described above,

$$\boldsymbol{M}_{\eta}(\boldsymbol{\eta})\ddot{\boldsymbol{\eta}} + \boldsymbol{C}_{\eta}(\boldsymbol{\eta}, \boldsymbol{\nu})\dot{\boldsymbol{\eta}} + \boldsymbol{D}_{\eta}(\boldsymbol{\eta})\dot{\boldsymbol{\eta}} + \boldsymbol{g}_{\eta}(\boldsymbol{\eta}) = \boldsymbol{\tau}_{\eta} + \mathrm{d}(t) \tag{39}$$

Using (24), the closed-loop equation becomes

$$\boldsymbol{M}_{\eta}(\boldsymbol{\eta})\dot{\boldsymbol{s}} + \boldsymbol{C}_{\eta}(\boldsymbol{\eta}, \boldsymbol{\nu})\boldsymbol{s} + \boldsymbol{\Gamma}\boldsymbol{s} = \mathrm{d}(t) \tag{40}$$

addition of $\boldsymbol{u}_0$ to the control law leads to

$$\boldsymbol{M}_{\eta}(\boldsymbol{\eta})\dot{\boldsymbol{s}} + \boldsymbol{C}_{\eta}(\boldsymbol{\eta}, \boldsymbol{\nu})\boldsymbol{s} + \boldsymbol{\Gamma}\boldsymbol{s} = \mathrm{d}(t) + \boldsymbol{u}_0 \tag{41}$$

To determine closed-loop stability, take $V = 0.5\boldsymbol{s}^{\mathrm{T}}\boldsymbol{M}\boldsymbol{s}$ to be the candidate Lyapunov function,

$$\dot{V} = -\boldsymbol{s}^{\mathrm{T}}\boldsymbol{\Gamma}\boldsymbol{s} + \boldsymbol{s}^{\mathrm{T}}\mathrm{d}(t) + \boldsymbol{s}^{\mathrm{T}}\boldsymbol{u}_0 \tag{42}$$

Now, by letting $\boldsymbol{u}_0 = -\chi\frac{\boldsymbol{s}}{\|\boldsymbol{s}\|}$,

$$\begin{aligned} \dot{V} &\leq -\underline{\lambda}(\boldsymbol{\Gamma})\|\boldsymbol{s}\|^2 + \chi\|\boldsymbol{s}\| + \boldsymbol{s}^{\mathrm{T}}\boldsymbol{u}_0 \\ &= -\underline{\lambda}(\boldsymbol{\Gamma})\|\boldsymbol{s}\|^2 \leq 0 \Rightarrow \boldsymbol{s} \rightarrow 0 \end{aligned} \tag{43}$$

Clearly, $\|\boldsymbol{u}_0\|$ is bounded in $[-\chi, \quad +\chi]$; however, as $\boldsymbol{s}$ goes through zero, chattering will ensue. To eliminate chattering, the additional term is modified as follows (see Theorem 14.1 and 14.2 in Khalil (2002)),

$$\boldsymbol{u}_0 = -\chi\tanh\left(\frac{\boldsymbol{s}}{\varepsilon}\right) \tag{44}$$

Since it is required to determine the upper bound of this disturbance, it is necessary to first characterize its constituent elements. The three main sources of uncertainty studied in this paper are modeling uncertainty, disturbances, and measurement error. Modeling parametric uncertainty refers to the mismatch between the estimated values and actual values of the model parameters such as added mass and the hydrodynamic coefficients and is denoted by $\boldsymbol{\tau}_p$. Disturbances refer to the various external and environmental forces such as wind, wind-generated waves, and ocean current that act on the ROV and are denoted by $\boldsymbol{\tau}_u$.

Finally, the torque error induced by the sensor measurement error is denoted by $\boldsymbol{\tau}_d$. In resume, taking into account the specified errors, the ROV's equation of motion in the body-fixed frame becomes

$$\boldsymbol{M}\dot{\boldsymbol{\nu}} + \boldsymbol{C}(\boldsymbol{\nu})\boldsymbol{\nu} + \boldsymbol{D}\boldsymbol{\nu} + \boldsymbol{g}(\boldsymbol{\eta}) = \boldsymbol{\tau} + \boldsymbol{\tau}_e \tag{45}$$

where

$$\boldsymbol{\tau}_e = \boldsymbol{\tau}_p + \boldsymbol{\tau}_u + \boldsymbol{\tau}_d \tag{46}$$

and $\boldsymbol{\tau}_p$, $\boldsymbol{\tau}_u$, and $\boldsymbol{\tau}_d$ are as specified previously.

3.3.1 Parametric Uncertainties

Let the error in the estimation of $\boldsymbol{M}_{\mathrm{RB}}$ and $\boldsymbol{M}_A$ be denoted by $\Delta\boldsymbol{M}$, the error in estimation of $\boldsymbol{C}(\boldsymbol{\nu})$ and $\boldsymbol{C}_A(\boldsymbol{\nu})$ be denoted by $\Delta\boldsymbol{C}$, and the error for $\boldsymbol{D}$ and $\boldsymbol{g}(\boldsymbol{\eta})$ be respectively denoted by $\Delta\boldsymbol{D}$ and $\Delta\boldsymbol{g}$. The upper bound for the estimation error of m, I_x, I_y, and I_z is assumed to be $\pm 100\varepsilon_1\%$. Thus, from (2) to (5), the largest percentage error in $\boldsymbol{M}_{\mathrm{RB}}$, $\boldsymbol{C}(\boldsymbol{\nu})$, and $\boldsymbol{g}(\boldsymbol{\eta})$ is $\pm 100\varepsilon_1$. Similarly, assuming the upper bound for the estimation error of the hydrodynamic coefficient is $\pm 100\varepsilon_2\%$, then the eventual model of the parametric uncertainty can be computed as follows:

$$\begin{aligned}
\Delta\boldsymbol{M} &= \pm\varepsilon_1\boldsymbol{M}_{\mathrm{RB}} \pm \varepsilon_2\boldsymbol{M}_A \\
\Delta\boldsymbol{C} &= \pm\varepsilon_1\boldsymbol{C}(\boldsymbol{\nu}) \pm \varepsilon_2\boldsymbol{C}_A(\boldsymbol{\nu}) \\
\Delta\boldsymbol{D} &= \pm\varepsilon_2\boldsymbol{D} \\
\Delta\boldsymbol{g} &= \pm\varepsilon_1\boldsymbol{g}(\boldsymbol{\eta}) \\
\Rightarrow \boldsymbol{\tau}_p &= \Delta\boldsymbol{M}\dot{\boldsymbol{\nu}} + \Delta\boldsymbol{C}\boldsymbol{\nu} + \Delta\boldsymbol{D}\boldsymbol{\nu} + \Delta\boldsymbol{g}
\end{aligned} \tag{47}$$

3.3.2 External Disturbances

Due to their stochastic nature, environmental disturbances are not usually included in ROV models. However, the benefit of the framework adopted in this paper is that it is possible to design the control law for some worst condition. The main environmental disturbances that are considered are wind-generated waves and ocean currents (Fossen 1994). Since it is assumed that the vessel is submerged, surface winds are not taken into consideration. The torque induced by the wind-generated waves and ocean currents are respectively denoted by τ_{wave} and τ_{current}. That is $\tau_u = \tau_{\mathrm{wave}} + \tau_{\mathrm{current}}$. The first component, τ_{wave}, may be modeled as follows (Fossen 1994):

$$\boldsymbol{\tau}_{\mathrm{wave}} = \begin{bmatrix} X_{\mathrm{wave}} & Y_{\mathrm{wave}} & Z_{\mathrm{wave}} & 0 & 0 & 0 \end{bmatrix}^{\mathrm{T}} \tag{48}$$

where

$$\begin{aligned}
X_{\mathrm{wave}} &= \sum_{i=0}^{N} \rho g B L T c(\rho) p_i(t) \\
Y_{\mathrm{wave}} &= -\sum_{i=0}^{N} \rho g B L T s(\rho) p_i(t) \\
N_{\mathrm{wave}} &= \sum_{i=0}^{N} \frac{1}{24} \rho g B L T \left(L^2 - B^2\right) s(2\rho) p_i^2(t)
\end{aligned} \tag{49}$$

Note that the forces induced by the waves (in (48)) are not so significant that required a torque generating pitch motion.

In (48), ρ (kg/m^3) is the density of the water, $B \times L$ (m^2) is the cross-sectional area of the ROV in water, T (m) is the draft distance, ρ is the angle between heading and the direction of the wave, and finally $p_i(t)$ is the wave slope for component i^{th} which can be obtained by statistical analysis such as short-term prediction. For the worst-condition case, the Pierson-Moskowitz (PM) spectrum gives

$$p_m = 0.0731\sqrt{\frac{V}{g}} \tag{50}$$

where V (in knots) is the wind speed at the height of 19.4 m over the sea surface and to have the worst case, the parameter ρ must be selected such that the maximum wave torque can be generated. Let the vertical position z be measured positive downward. From (48) and ignoring surface winds, one arrives at

$$\begin{aligned}
\boldsymbol{\tau}_{\mathrm{wave}}^{\mathrm{T}} &= \frac{\rho g p_m N B L T u_{-1}(0.5 - z)}{24} \\
&\begin{bmatrix} 24c(\rho) & -24s(\rho) & \left(L^2 - B^2\right)p_m s(2\rho) & 0 & 0 & 0 \end{bmatrix}
\end{aligned} \tag{51}$$

where $u_{-1}(.)$ is the Heaviside function and $z \geq 0$. As the ocean current uncertainty is assumed to be continuous, its effect may be reproduced by varying the relative velocity in (6). The relative velocity is defined as $\boldsymbol{\nu}_r = \boldsymbol{\nu} - \boldsymbol{\nu}_c$, where $\boldsymbol{\nu}_{\mathrm{c}}$ is the current velocity in the body-fixed reference. In this case, the current velocity will be measured by an acoustic Doppler current profiler (ADCP). If the body-fixed current velocity is constant or slowly varying, then

$$\ddot{\boldsymbol{v}}_c = 0 \Rightarrow \ddot{\boldsymbol{v}}_r = \ddot{\boldsymbol{v}} \tag{52}$$

and the nonlinear relative equation of motion becomes

$$\begin{gathered} \boldsymbol{M}\dot{\boldsymbol{\nu}} + \boldsymbol{C}(\boldsymbol{\nu}_r)\boldsymbol{\nu}_r + \boldsymbol{D}\boldsymbol{\nu}_r + \boldsymbol{g}(\boldsymbol{\eta}) = \boldsymbol{\tau} \Rightarrow \\ \boldsymbol{M}\dot{\boldsymbol{v}} + \boldsymbol{C}(\boldsymbol{\nu})\boldsymbol{\nu} + \boldsymbol{D}\boldsymbol{\nu} + \boldsymbol{g}(\boldsymbol{\eta}) = \boldsymbol{C}(\boldsymbol{\nu})\boldsymbol{\nu} - \boldsymbol{C}(\boldsymbol{\nu}_r)\boldsymbol{\nu}_r + \boldsymbol{D}\boldsymbol{\nu}_c + \boldsymbol{\tau} \end{gathered} \tag{53}$$

From (3) to (5), it is evident that the Coriolis and centripetal matrix is a linear operator on the velocity. Thus, the current-induced moments may be modeled as

$$\boldsymbol{\tau}_{\text{current}} = \boldsymbol{C}(\boldsymbol{\nu})\boldsymbol{\nu}_{\text{c}} + \boldsymbol{C}(\boldsymbol{\nu}_{\text{c}})\boldsymbol{\nu}_{\text{r}} + \boldsymbol{D}\boldsymbol{\nu}_c \tag{54}$$

where $\boldsymbol{\nu}_{\text{c}} = [u_c \;\; v_c \;\; w_c \;\; 0 \;\; 0 \;\; 0]^{\text{T}}$ is a vector of non-rotational body-fixed current velocities (Fossen 1994). The value of $\boldsymbol{\nu}_{\text{c}}$ can be determined by using the IET from the earth-fixed frame $\boldsymbol{\nu}_{\mathbf{c}}^E = \begin{bmatrix} u_c^E & v_c^E & w_c^E & 0 & 0 & 0 \end{bmatrix}^{\text{T}}$ as follows: let α_1 and α_2 be defined as angle of attack and sideslip that describe the orientation of the current velocity profile ($V_c(z)$). Then,

$$\begin{aligned} u_c^E &= V_c c(\alpha_1)c(\alpha_2) \\ v_c^E &= V_c s(\alpha_2) \\ w_c^E &= V_c s(\alpha_1)c(\alpha_2) \end{aligned} \tag{55}$$

The six velocity components may then be written as a single summation $V_c(z)$, where it is noted that the first three components are often the dominant terms (Williams et al. 2000) for ROV operating above the seabed above the pipeline,

$$\begin{aligned} V_c(z) = V_t(z) + V_{lw}(z) + V_s(z) = V_t(0) \\ + V_{lw}(0)\left(\frac{d_0 - z}{d_0}\right)u_{-1}(50 - z) + 0.0286\left(\frac{V^2}{g}\right)e^{-\frac{gz}{V^2}} \end{aligned} \tag{56}$$

where V_t is the tidal component, V_{lw} is the component generated by local winds, and V_s is the Stokes drift component (due to nonlinear waves). Finally, $\boldsymbol{\nu}_{\text{c}} = \begin{bmatrix} \nu_{c_1}^{\text{T}} & \nu_{c_2}^{\text{T}} \end{bmatrix}^{\text{T}}$ is obtained as follows:

$$\boldsymbol{\nu}_{\text{c}_1} = \boldsymbol{J}_1^{-1}(\boldsymbol{\eta}) \begin{bmatrix} c(\alpha_1)c(\alpha_2) \\ s(\alpha_2) \\ s(\alpha_1)c(\alpha_2) \end{bmatrix} V_c(z) \quad , \quad \boldsymbol{\nu}_{\text{c}_2} = [0 \;\; 0 \;\; 0]^{\text{T}} \tag{57}$$

3.3.3 Measurement Error

In computation of the SMC law, the exact values of $\boldsymbol{\eta}$ and $\dot{\boldsymbol{\eta}}$ are required. In reality, these terms are measured using the accelerometer and the gyroscope. Even in the best cases, these measurements will not be perfect. The significance of these errors is that even negligible errors in the measurements may produce a large error in the value of $\boldsymbol{\eta}$ and $\dot{\boldsymbol{\eta}}$ as these are obtained by integrating the velocity ($\boldsymbol{\nu}_2$) and acceleration ($\dot{\boldsymbol{\nu}}_1$) of the ET. To determine the effects of these errors, let the inertial sensor measurements be $\dot{\boldsymbol{\nu}}_1 + \boldsymbol{e}_1$ and $\boldsymbol{\nu}_2 + \boldsymbol{e}_2$, where $\boldsymbol{e}_1$ and $\boldsymbol{e}_2$ are measurement errors,

$$\boldsymbol{e}_1 = \pm\varepsilon_3\dot{\boldsymbol{\nu}}_1 \quad \& \quad \boldsymbol{e}_2 = \pm\varepsilon_4\boldsymbol{\nu}_2 \tag{58}$$

From (23), this error can be modeled by an additional force on the right hand side of (6) where the effect of the inflow velocity to the thruster blades is assumed to be negligible. Let the added term be denoted by τ_d,

$$\begin{aligned} \boldsymbol{\tau}_d = \boldsymbol{J}^{\text{T}}(\boldsymbol{\eta})\Big(\boldsymbol{M}_\eta(\boldsymbol{\eta})\,\dot{\vartheta} + \boldsymbol{C}_\eta(\boldsymbol{\eta},\boldsymbol{\nu})\vartheta + \boldsymbol{D}_\eta(\boldsymbol{\eta})\boldsymbol{\nu} + \boldsymbol{g}_\eta(\boldsymbol{\eta}) - \boldsymbol{\Gamma}\boldsymbol{s} \\ - \boldsymbol{M}_\eta(\hat{\boldsymbol{\eta}})\,\dot{\vartheta} - \boldsymbol{C}_\eta(\hat{\eta},\hat{\nu})\hat{\vartheta} - \boldsymbol{D}_\eta(\hat{\boldsymbol{\eta}})\hat{\boldsymbol{\nu}} - \boldsymbol{g}_\eta(\hat{\boldsymbol{\eta}}) + \boldsymbol{\Gamma}\hat{\boldsymbol{s}}\Big) \end{aligned} \tag{59}$$

where, by assumption of constant ε_3 and ε_4, it leads to

$$\dot{\boldsymbol{\eta}}(t) = \boldsymbol{J}(\hat{\boldsymbol{\eta}}(t)) \begin{bmatrix} \int_0^t \dot{\boldsymbol{\nu}}_1(\tau)(1 \pm \varepsilon_3)\;\mathrm{d}\tau \\ \boldsymbol{\nu}_2(t)(1 \pm \varepsilon_4) \end{bmatrix} = \boldsymbol{J}(\hat{\boldsymbol{\eta}}(t)) \begin{bmatrix} \boldsymbol{\nu}_1(t)(1 \pm \varepsilon_3) \\ \boldsymbol{\nu}_2(t)(1 \pm \varepsilon_4) \end{bmatrix} \tag{60}$$

The terms $\hat{\vartheta}$ and $\hat{\boldsymbol{s}}$ will be obtained by inserting the above equality in (24).

3.4 Bound of Uncertainties

To robustify the controller, the upper bound of the uncertainty in the Earth-fixed reference equations of motion is required, i.e.,

$$\chi = \max_t \|\mathrm{d}(t)\| = \max_t \|\boldsymbol{J}^{-\text{T}}(\boldsymbol{\eta}(t))\boldsymbol{\tau}_{\text{e}}\| \tag{61}$$

Due to the stochastic nature of some of constituent elements, finding an exact value for χ might not be possible. But a good estimate can be obtained by providing certain uncertainties or errors in simulation. Traditionally, the effects of these disturbances are dealt with by incorporating an adaptive element in the control law (Qiao and Zhang 2017; Yin et al. 2003; Effatnejad and Namvar 2009;Valdovinos et al. 2009). However, as previously described in the introduction, in this work, the control law is made robust against these changes, instead of being made adaptive. A number of reasons warrant this decision: Firstly, making the control law adaptive will bring with it an increased computational burden which may be required to be carried out on-board. This will increase further, if reasonably fast tracking dynamics are required. Secondly, since in pipeline tracking, the location of the task space is fixed, a good estimate for d_0, $V_t(0)$, V, and $\boldsymbol{g}$ can be determined

a priori. Moreover, information on the maximum measurement error is readily available from the manufacturer. Finally, disturbances will usually violate any slow-varying condition required to convergence. Therefore, by noting the convergence of the SMC trajectory tracking error to zero, the upper bound of $\|\boldsymbol{d}(t)\|$ can be represented in terms of ε_i as

$$\chi = \max_t \|\boldsymbol{J}^{-1}(\boldsymbol{\eta}_d(t))\boldsymbol{\tau}_e^d\| \tag{62}$$

where $\boldsymbol{\tau}_e^d$ is the expected extra torque in the body-fixed equation of the motion, with $\boldsymbol{\eta} = \boldsymbol{\eta}_d$, $\dot{\boldsymbol{\eta}} = \dot{\boldsymbol{\eta}}_d$, and $\boldsymbol{\nu} = \boldsymbol{\nu}_d$.

4 Pipeline Simulation Results

For previous studies on the Pipeline tracking problem, please refer to the following references (Curti et al. 2005; Calvo et al. 2009; Chin et al. 2011). The main purpose of pipeline tracking is autonomous inspections with minimum human intervention. The advantage of using AUV in pipeline inspection is its minimum human intervention required. However, the current generation of AUV is still not as successful or useful as the ROVs. Mainly, this is due to the fact that a hard-wire link for delivery of suitable power supply and real-time image processing is still required. Moreover, wireless communication in water is

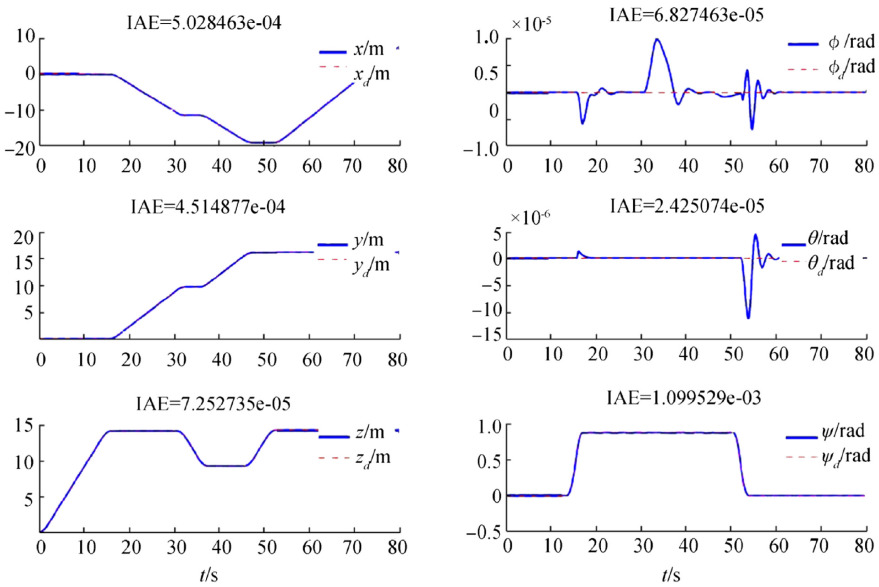

(a) Position and orientation tracking - (m and rad) vs. time (s) – without uncertainty

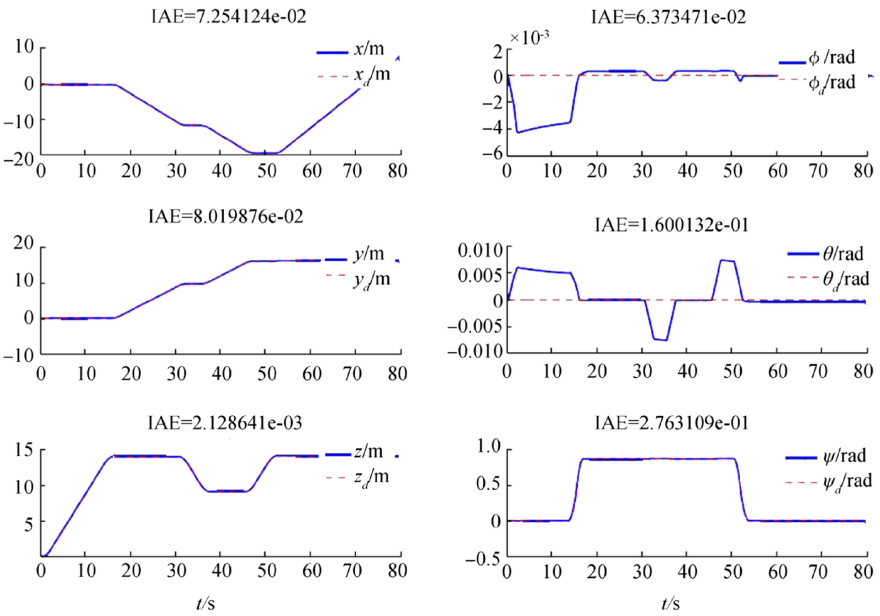

(b) Position and orientation tracking - (m and rad) vs. time (s) – in the presence of uncertainty

Fig. 3 Position and orientation tracking — (m and rad) vs. time (sec) (**a**) without uncertainty (**b**) with presence of uncertainity

seriously hampered by the Doppler effect which limits both the rate and the range of possible communications.

The RRC ROV model, uncertainty, and controller parameters used to set up the simulation are given in Appendix Tables 2, 3, and 4. Numerous simulations have been run to assess the performance of the ROV. All simulations are performed in MATLAB SIMULINK software. Due to lack of space, only one set for each of the uncertain and certain cases is presented in Figs. 3, 4, 5, and 6. For each instance, the value of tracking integral absolute error (IAE) is indicated on the plot itself. Variables x and y represent longitude and latitude coordinate in all figures, while z denotes altitude which is positively downward.

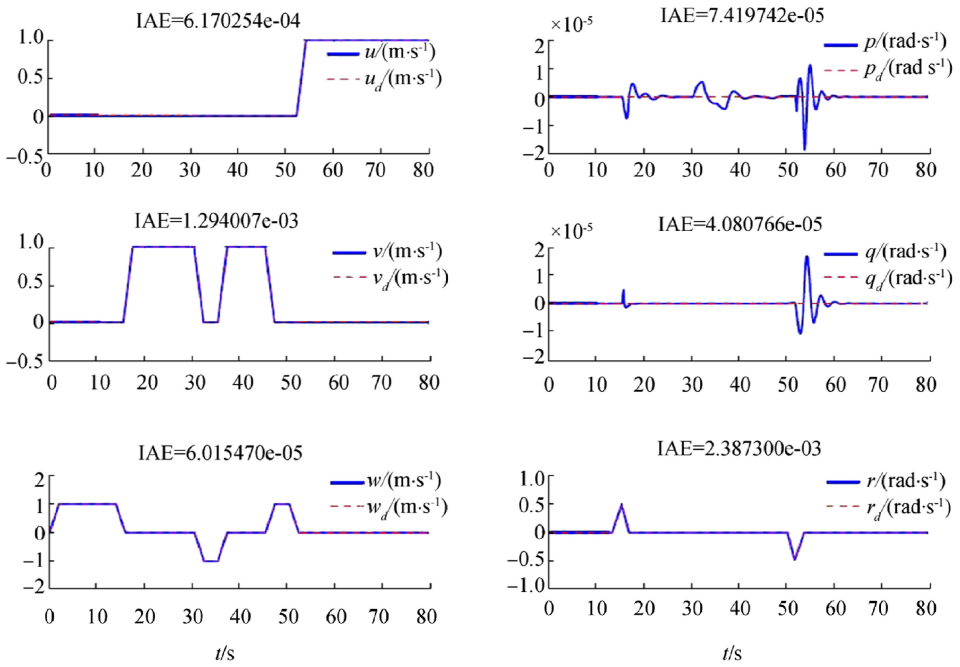

Fig. 4 Velocity tracking in body-fixed coordinate — (m/sec and rad/s) vs. time (sec) (**a**) without uncertainty (**b**) with presence of uncertainity

(a) Velocity tracking in body-fixed coordinate - (m/s and rad/s) vs. time (s)- without uncertainty

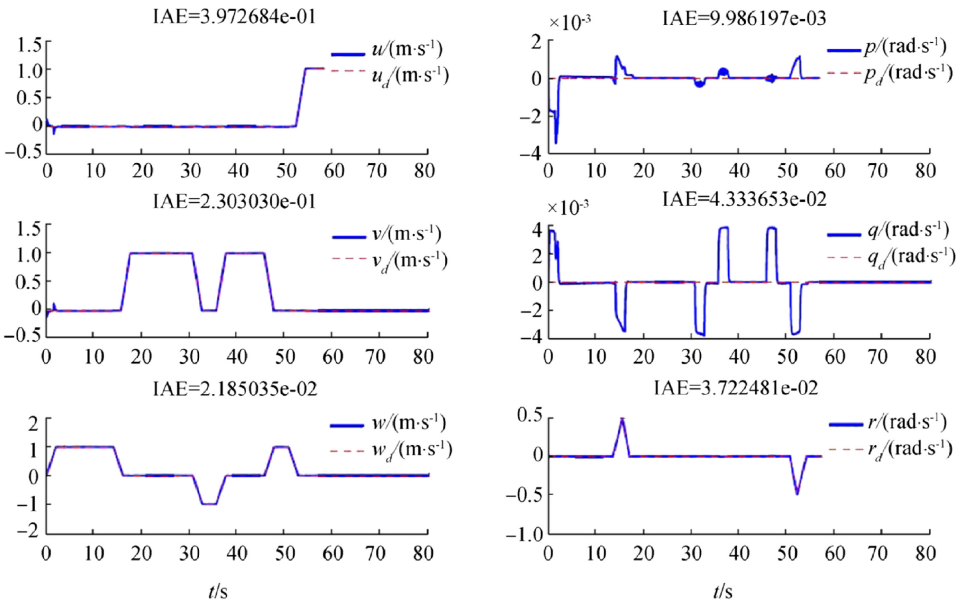

(b) Velocity tracking in body-fixed coordinate - (m/s and rad/s) vs. time (s)- in the presence of uncertainty

4.1 Robust Position, Orientation Tracking, and Thrust Results

Figure 3 shows the position and orientation of tracking in the earth-fixed reference frame (η and η_d) and Fig. 4 displays velocity tracking in body-fixed coordinated frame (ν and ν_d). The optimal required thrusts for this path are depicted in Fig. 5a, b for the certain and uncertain cases respectively. The results show that the ROV can track the pipelines robustly.

4.2 Robust 3D Tracking Results

Figure 6 shows a 3D view of the desired and actual ROV trajectory. This figure graphically verifies the performance of the controller in light of the main pipeline inspection objectives, i.e., tracking with minimal error.

While the controller gives excellent tracking performance even in the case of considering the worst-case combination of all uncertainties, as expected this does comes at the expense of requiring larger torques from the thrusters. This is logical since additional torque is required to counter the effects of uncertainties. It is also necessary to point out that the control law momentarily violates the maximum torque specification of the thrusters. However, the overload is of a limited duration and is not considered to be of a critical nature. It is also important to consider how the torque profiles change in the simulation of the uncertainty system. Initially, it is thrusters 3 and 4 which see the biggest change. This is due to the effect of wind-generated wave and ocean current direction which cause large disturbances in the z direction. However, as the ROV proceeds along the desired trajectory, the disturbances in the x and y direction become more pronounced, leading to changes in the torque profile of thrusters 1 and 2.

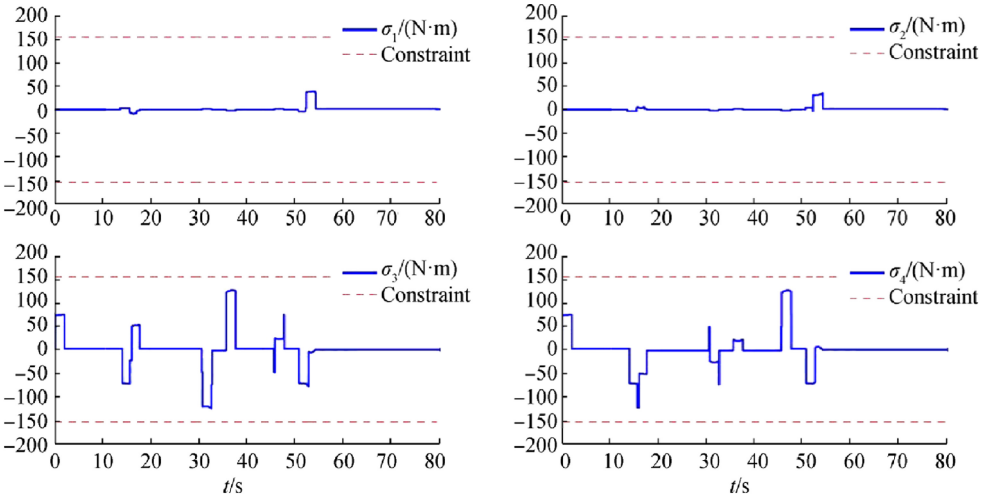

(a) Required thrust and their limits - (Nm) vs. time (s) - without uncertainty

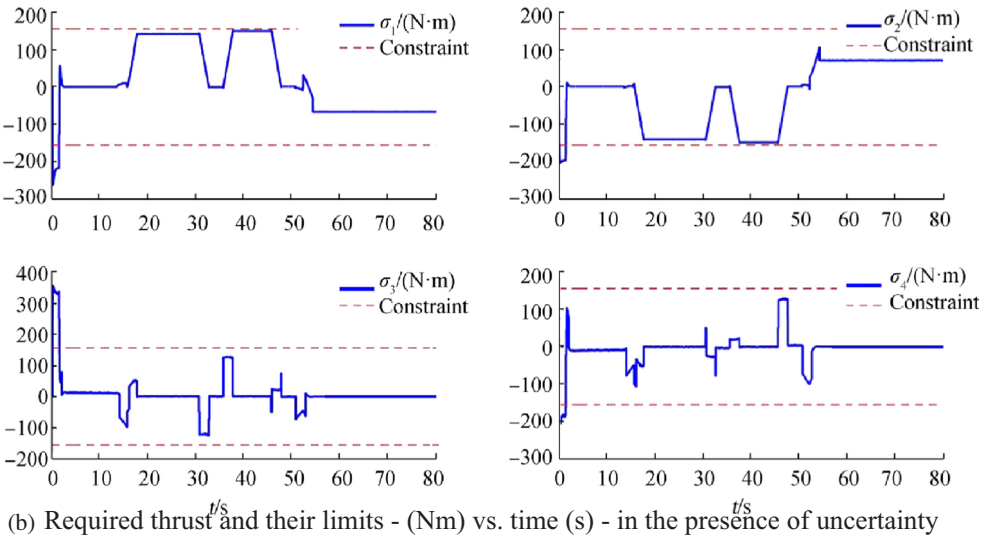

(b) Required thrust and their limits - (Nm) vs. time (s) - in the presence of uncertainty

Fig. 5 Required thrust and their limits — (Nm) vs. time (sec) (**a**) without uncertainty (**b**) with presence of uncertainity

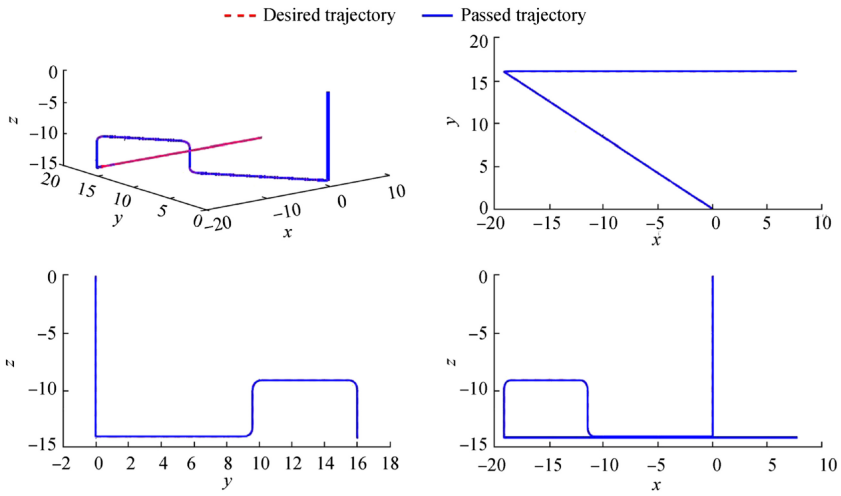

(a) Trajectory tracking - (m× m× m)- without uncertainty

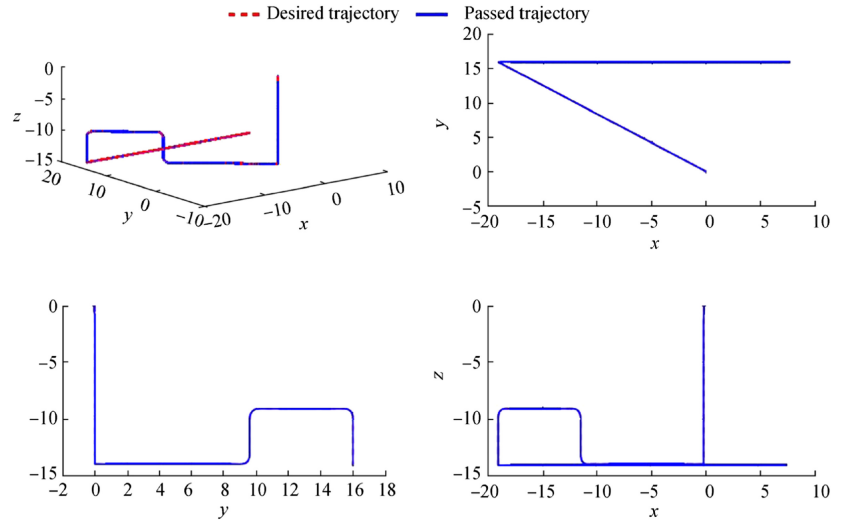

(b) Trajectory tracking - (m× m× m)- in the presence of uncertainty

Fig. 6 Trajectory tracking — (m x m x m) (**a**) without uncertainty (**b**) with presence of uncertainty

5 Conclusions

The paper described modeling, sliding-mode control (SMC) design, and simulation of the RRC ROV. The dynamic model of the ROV was obtained from both CFD software and experimental techniques performed in the swimming pool and water tank tests. These experimental tests were performed to verify the damping and added mass coefficients used in the dynamic equations. The results from the CFD software (such as ANSYS™, MULTISURF™, and WAMIT™ software) were verified by comparing them to a free-decaying experiment on a scaled RRC ROV model. By applying laws of similitude, the hydrodynamics damping and added mass forces or the coefficients of the scaled model were scaled up to predict the corresponding values of the actual RRC ROV model.

The sliding-model control law was first developed and then made robust against uncertainties with a known bound. The bound for the uncertainties was obtained from a detailed analysis of environmental disturbance's modeling and was then verified through simulation of the real-life model of the ROV on a path-following mission. The simulated results showed an excellent tracking performance with the minimal position tracking error. For future works, other approaches such as machine learnings will be applied on the ROV. Experimental works to test the control scheme will be implemented.

Acknowledgements The author would like to express his thanks to Newcastle University in Singapore campus for providing the support during the project.

Appendix

Table 1 Damping and added mass coefficients used for RRC ROV model simulation

Methods	Damping coefficient/added mass coefficient							
	Surge (0–0.5 m/s)		Sway (0–0.5 m/s)		Heave (0–0.02 m/s)		Yaw (0–0.5 rad/s)	
	X_u	$X_{u\mid u\mid}$	Y_v	$Y_{v\mid v\mid}$	Z_w	$Z_{w\mid w\mid}$	N_r	$N_{r\mid r\mid}$
ANSYS-CFX	11.863	108.45	19.640	108.24	2.3756	351.98	0	10.390
Experiment	17.240	106.03	38.060	84.100	72.530	104.41	1.180	7.5100
	X_u		Y_v		Z_w		N_r	
WAMIT	21.140		51.700		92.450		2.3030	
Experiment	21.480		55.170		113.60		0.2960	

Table 2 Parameters for ROV model

Parameters	Values
$\boldsymbol{M}_{\mathrm{RB}}$	[115 0 0 0 0 0 01150000 00115000 0006.1−0.00016−0.185 000−0.000165.980.0006 000−0.1850.00065.517]
M_A	diag([21.1403, 51.7012, 92.4510, 3.6191, 2.6427, 2.3033])
$\boldsymbol{C}_{12}(\nu)$	[0 115w −115v −115w0115u 115v−115u0]
$\boldsymbol{C}_{22}(\nu)$	[−0.0006q + 0.185p + 5.5170r −0.0006q + 0.185p + 5.5170r 0.0006r−0.0002p−5.9800q 0.0006q−0.185p−5.5170r00.1850r +0.0002q + 6.100p −0.0006r + 0.0002p + 5.9800q−0.1850r−0.0002q−6.100p0]
$\boldsymbol{C}_A(\nu)$	[0 0 0 0 −92.4510w 51.7012v 00092.4510w0−21.140u 000−51.7012v21.140u0 0−92.4510w51.7012v0−2.3033r2.6427q 92.4510w0−21.140u2.3033r0−3.6191p −51.7012v21.140u0−2.6427q3.6191p0]
$\boldsymbol{D}$	diag([17.2, 38.06, 72.50, 1.665, 1.456, 1.180])
$\boldsymbol{W}$	115 (kg)
$\boldsymbol{r}_G$	$[x_G, y_G, z_G]^{\mathrm{T}} = [0, 0, 0]^{\mathrm{T}}$ (m)
$\boldsymbol{r}_B$	$[x_B, y_B, z_B]^{\mathrm{T}} = [0, 0, -0.048]^{T}$ (m)
$\boldsymbol{T}$	[1 1 0 0 000.707−0.707 000.7070.707 00−0.2930.293 −0.016−0.0160.012−0.012 0.31−0.310.012−0.012]

Table 3 Parameters used in computing uncertainties

Parameter	ρ	V	ρ	α_1	α_2	V_{10}	d_0	$V_t(0)$	ε_1	ε_2	ε_3	ε_4
Value	1000	10	π/4	π/12	π/4	5.15	50	0.8	0.01	0.1	0.001	0.01
Unit	kg/m^3	kn	rad	rad	rad	m/s	m	m/s	–	–	–	–

Table 4 Controller gains and parameters used

Controller gains and parameters	Without uncertainty	With uncertainty
λ_i, i = 1, 2, …, 6	10	10
γ_i, i = 1, 2, …, 6	10	5
χ	0	608
ε	0	0.5

References

Antonelli G, Chiaverini S, Sarkar N, West M (2001) Adaptive control of an autonomous underwater vehicle: experimental results on ODIN. IEEE Trans Control Syst Technol 9(5):756–765. https://doi.org/10.1109/87.944470

Burkan R, Uzmay I (2003) Upper bounding estimation for robustness to the parameter uncertainty in trajectory control of robot arm. Robot Auton Syst 45(2):99–110. https://doi.org/10.1007/s10846-006-9061-5

Caccia M, Indiveri G, Veruggio G (2000) Modeling and identification of open-frame variable configuration unmanned underwater vehicles. IEEE J Ocean Eng 25(2):227–240. https://doi.org/10.1109/48.838986

Calvo O, Sousa A, Rozenfeld A, Acosta G (2009) Smooth path planning for autonomous pipeline inspections. 6th International Multi-Conference on Systems, Signals and Devices SSD'09, pp 1–9. https://doi.org/10.1109/SSD.2009.4956800.

Chiaverini S, Antonelli G, Caccavale F (2004) Adaptive tracking control of underwater vehicle-manipulator systems based on the virtual decomposition approach. IEEE Trans Robot Autom 20(3):594–602. https://doi.org/10.1109/TRA.2004.825521

Chin CS, Lin WP (2018) Robust genetic algorithm and fuzzy inference mechanism embedded in sliding-mode controller for uncertain underwater robot. IEEE/ASME Trans Mechatronics 23(2):655–666. https://doi.org/10.1109/TMECH.2018.2806389

Chin CS, Lau MWS, Low E (2011) Supervisory cascaded controller design: experiment test on a remotely operated vehicle. Proc Inst Mech Eng C J Mech Eng Sci 225(3):584–603. https://doi.org/10.1243/09544062JMES2223

Curti HJ, Acosta GG, Calvo OA (2005) Autonomous underwater pipeline inspection in autotracker project: the simulation module. In Oceans 2005-Europe, volume 1, 384–388. https://doi.org/10.1109/OCEANSE.2005.1511745.

Effatnejad K, Namvar M (2009) Adaptive robust control of robot manipulators subject to input-dependent uncertainties. 4th IEEE Conference on Industrial Electronics and Applications, pp 3428–3433. https://doi.org/10.1109/ICIEA.2009.5138838

Ferziger JH, Perić M (2002) Computational methods for fluid dynamics, volume 3. Springer, Berlin ISBN 978-3-642-56026-2

Fossen TI (1994) Guidance and control of ocean vehicles. Wiley ISBN: 978-0-471-94113-2

Islam S, Liu XP (2011) Robust sliding mode control for robot manipulators. IEEE Trans Ind Electron 58(6):2444–2453. https://doi.org/10.1109/TIE.2010.2062472

Jordán MA, Bustamante JL (2007) Numerical stability analysis and control of umbilical–ROV systems in one-degree-of-freedom taut–slack condition. Nonlinear Dynamics 49(1–2):163–191. https://doi.org/10.1007/s11071-006-9120-2

Khalil HK (2002) Nonlinear systems, volume 3. Prentice hall Upper Saddle River ISBN-13:978–0130673893

Koh TH, Lau MWS, Low E, Seet G, Swei S, Cheng PL (2002) Development and improvement of an underactuated underwater robotic vehicle, OCEANS '02 MTS. IEEE 4:2039–2044. https://doi.org/10.1109/OCEANS.2002.1191945.

Liang X, Wang H, Liu YH, Chen W, Hu G, Zhao J (2016) Adaptive task-space cooperative tracking control of networked robotic manipulators without task-space velocity measurements. IEEE Trans Cybern 46(10):2386–2398. https://doi.org/10.1109/TCYB.2015.2477606

McLain TW and Rock SM (1996) Experiments in the hydrodynamic modeling of an underwater manipulator. Proceedings of the 1996 Symposium on Autonomous Underwater Vehicle Technology, pp 463–469. https://doi.org/10.1109/AUV.1996.532448.

Medina YV, Tkachova AF, Santana LH, Entenza PJP (2016) Yaw controller in sliding mode for underwater autonomous vehicle. IEEE Lat Am Trans 14(3):1213–1220. https://doi.org/10.1109/TLA.2016.7459601

Monroy JA, Campos E, Torres JA (2017) Attitude control of a micro AUV through an embedded system. IEEE Lat Am Trans 15(4):603–612. https://doi.org/10.1109/TLA.2017.7896344

Nicholas LT, Valladarez D, Toit NED (2015) Robust adaptive control of underwater vehicles for precision operations. In OCEANS 2015 - MTS/IEEE. https://doi.org/10.23919/OCEANS.2015.7404364

Qiao L, Zhang W (2017) Adaptive non-singular integral terminal sliding mode tracking control for autonomous underwater vehicles. IET Control Theory Appl 11(8):1293–1306. https://doi.org/10.1049/iet-cta.2017.0016

Shen C, Buckham B, Shi Y (2017a) Modified C/GMRES algorithm for fast nonlinear model predictive tracking control of AUVs. IEEE Trans Control Syst 25(5):1896–1904. https://doi.org/10.1109/TCST.2016.2628803

Shen C, Shi Y, Buckham B (2017b) Integrated path planning and tracking control of an AUV: a unified receding horizon optimization approach. IEEE/ASME Trans Mechatronics 22(3):1163–1173. https://doi.org/10.1109/TMECH.2016.2612689

Shi Y, Shen C, Fang H, Li H (2017) Advanced control in marine mechatronic systems: a survey. IEEE/ASME Trans Mechatronics 22(3):1121–1131. https://doi.org/10.1109/TMECH.2017.2660528

Skogestad S, Postlethwaite I (2005) Multivariable feedback control: analysis and design, 2nd edn. Wiley, Hoboken ISBN: 978-0-470-01167-6

Slotine JJE, Li W (1991) Applied nonlinear control, volume 199. Prentice Hall, New Jersey ISBN-13: 978–0130408907

Tang C, Wang Y, Wang S, Wang R, Tan M (2018) Floating autonomous manipulation of the underwater biomimetic vehicle-manipulator system: methodology and verification. IEEE Trans Ind Electron 65(6):4861–4870. https://doi.org/10.1109/TIE.2017.2772148

Valdovinos LGG, Jimenez TS, Rodriguez HT (2009) Model-free high order sliding mode control for rov: station-keeping approach. In OCEANS 2009, MTS/IEEE Biloxi—marine technology for our future: global and local challenges, pp 1–7. https://doi.org/10.23919/OCEANS.2009.5422455

Vasilijevic A, Nad D, Mandic F, Miskovic N, Vukic Z (2017) Coordinated navigation of surface and underwater marine robotic vehicles for ocean sampling and environmental monitoring. IEEE/ASME Trans Mechatronics 22(3):1174–1184. https://doi.org/10.1109/TMECH.2017.2684423

Vázquez AJM, Rodríguez HR, Vega VP, Orta AS (2017) Fractional sliding mode control of underwater rovs subject to non-differentiable disturbances. Int J Control Autom Syst 15:1314–1321. https://doi.org/10.1007/s12555-015-0210-0

Williams C, Mackay M, Perron C, Muselet C (2000) The NRC-IMD marine dynamics test facility: a six-degree-of freedom forced-motion apparatus for underwater vehicle testing. NRC Institute for Ocean Technology; National Research Council Canada, IR-1999-28

Wilson R, Paterson E, Stern F (2006) Unsteady rans CFD method for naval combatant in waves. Proceedings of the 22nd ONR Symposium on Naval Hydrodynamics, pp 532–549. https://doi.org/10.1002/fld.183

Yin Y, Hayakawa Y, Ogata K, Hosoe S (2003) A nonlinear adaptive robust control design for robotic systems under time-varying parameter perturbation and external disturbance. Proceedings of IEEE/RSJ International Conference on Intelligent Robots and Systems, pp 2767–2772. https://doi.org/10.1109/IROS.2003.1249289